Journal of Thermal Analysis and Calorimetry, Vol. 89 (2007) 2, 417–425

INVESTIGATION OF THE RIGID AMORPHOUS FRACTION IN NYLON-6

H. Chen and Peggy Cebe[*]

Department of Physics and Astronomy, Tufts University, Medford, MA 02155, USA

A three-phase model, comprising crystalline, mobile amorphous, and rigid amorphous fractions (χ_c, χ_{MA}, χ_{RA}, respectively) has been applied in the study of semicrystalline Nylon-6. The samples studied were Nylon-6 alpha phase prepared by subsequent annealing of a parent sample slowly cooled from the melt. The treated samples were annealed at 110°C, then briefly heated to 136°C, then re-annealed at 110°C. Temperature-modulated differential scanning calorimetry (TMDSC) measurements allow the devitrification of the rigid amorphous fraction to be examined.

We observe a lower endotherm, termed the 'annealing' peak in the non-reversing heat flow after annealing at 110°C. By brief heating above this lower endotherm and immediately quenching in LN_2-cooled glass beads, the glass transition temperature and χ_{RA} decrease substantially, χ_{MA} increases, and the annealing peak disappears. The annealing peak corresponds to the point at which partial de-vitrification of the rigid amorphous fraction (RAF) occurs. Re-annealing at 110°C causes the glass transition and χ_{RA} to increase, and χ_{MA} to decrease. None of these treatments affected the measured degree of crystallinity, but it cannot be excluded that crystal reorganization or recrystallization may also occur at the annealing peak, contributing to the de-vitrification of the rigid amorphous fraction.

Using a combined approach of thermal analysis with wide and small angle X-ray scattering, we analyze the location of the rigid amorphous and mobile amorphous fractions within the context of the Heterogeneous and Homogeneous Stack Models. Results show the homogeneous stack model is the correct one for Nylon-6. The cooperativity length (ξ_A) increases with a decrease of rigid amorphous fraction, or, increase of the mobile amorphous fraction. Devitrification of some of the RAF leads to the broadening of the glass transition region and shift of T_g.

Keywords: *Nylon-6, rigid amorphous fraction (RAF), TMDSC*

Introduction

Depending upon thermal history, Nylon-6 crystallizes into two crystallographic forms: monoclinic alpha phase, and hexagonal/pseudohexagonal gamma phase. In general, rapid cooling or quenching from the melt produces the gamma phase, while slow cooling yields alpha phase [1]. Gamma phase is unstable, and will undergo cold crystallization at room temperature and transform to alpha phase when heated up to about 150°C [1, 2]. The alpha phase is stable before melting, and temperature modulated differential scanning calorimetry (TMDSC) can be used to assess its glass transition relaxation and melting behavior.

Recent studies suggest that there are three fractions in semicrystalline Nylon-6: the crystalline, C, the mobile amorphous, MAF, and the rigid amorphous, RAF, fractions [3–5]. Like other semicrystalline polymers such as poly(ethylene terephthalate), PET [6], poly(etheretherketone), PEEK [7], poly(phenylene sulfide), PPS [8], and isotactic polystyrene, iPS [9, 10], in semicrystalline Nylon-6 only the mobile amorphous fraction undergoes the glass transition relaxation and becomes liquid-like just above T_g. The crystalline and rigid amorphous factions remain solid-like within a certain temperature range above T_g. Below T_g all the three fractions are solid-like.

PET [6], PPS [8] and iPS [9, 10] show two melting endotherms after isothermal crystallization or annealing at a temperature between T_g and the melting temperature. In PET, Song stated that the relaxation of RAF occurred between the glass transition and the pre-melting peak, i.e., the lowest endotherm seen in the DSC scan, also termed the 'annealing peak' [9] and occurring at temperature T_a. For iPS [10] and poly(phenylene oxide), PPO [11], the rigid amorphous fraction was considered to relax only after melting the crystals. For poly(3-hydroxybutyrate), PHB, poly(carbonate), PC [12, 13], and iPS [9], the RAF formed at the crystallization temperature and was relaxed at the lowest endotherm.

Two competing models exist to describe the organization of the polymer lamellae within the spherulites, viz., the 'Heterogeneous Stack Model', HET [14, 15], and the 'Homogeneous Stack Model', HSM [15–19]. The nature of the lamellar structure, whether

* Author for correspondence: peggy.cebe@tufts.edu

1388–6150/$20.00

Akadémiai Kiadó, Budapest, Hungary
Springer, Dordrecht, The Netherlands

lamellae are space filling or not, determines whether the HET or HSM is appropriate for a given polymer. HET makes the assumption that the entire mobile amorphous region is outside the lamella stacks and the RAF is the only amorphous material located between adjacent lamellae. On the other hand, in the HSM, the mobile amorphous region is inside the lamella stack and the rigid amorphous material is an interfacial layer between the lamellae and the MAF. These models will be described more completely in 'Lamellar structural model for Nylon-6'.

Small angle X-ray scattering (SAXS) alone cannot distinguish between these models, in which Babinet's principle of reciprocity prevents association of the crystal and amorphous phases with the longer or shorter of the two correlation lengths within the lamellar stacks. Here we combine thermal analysis and SAXS to determine the location of RAF and MAF within the context of these two models.

In the present work on the crystalline alpha phase of Nylon-6, we examine the behavior of the crystal, mobile amorphous, and rigid amorphous fractions after annealing at 110°C. We demonstrate that a portion of RAF can be devitrified by brief heating to a temperature above the annealing peak; however, not all the RAF is relaxed by heating above T_a. RAF can be reformed by re-annealing the sample at 110°C. The impact of these treatments on the crystal fraction and the glass transition temperature is determined. Using a combination of thermal and structural analysis to investigate the location of the rigid amorphous and mobile amorphous fractions in semicrystalline Nylon-6, the results demonstrate that HSM is the correct model for Nylon-6.

Experimental

Nylon-6 (resin grade 8082) was obtained from Honeywell in pellet form. The resin was compression-molded at 250°C for 3 min to remove the prior thermal history, and then quenched in liquid nitrogen (LN_2) to obtain the film. Sample A is the film held at 280°C for 3 min and then cooled to room temperature in a Mettler hot stage at a slow cooling rate of 5°C min^{-1}. Sample A is the parent for the next three-sample treatments:

B1 is Sample A heated to 110°C at 5°C min^{-1} and annealed for 10 min and then immediately quenched in LN_2–cooled glass beads, a good thermal conductor.

B2 is prepared as Sample B1, but after the annealing step at 110°C, the sample was heated momentarily to 136°C at 20°C min^{-1}, then immediately quenched in LN_2–cooled glass beads.

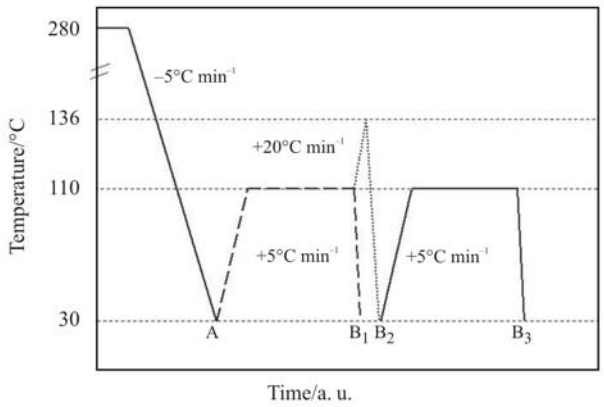

Fig. 1 Temperature *vs*. time scheme for sample preparation. A (solid line at early time) is the parent sample for subsequent treatments B1, B2 and B3 (solid). The heating rates are indicated; the cooling rate was rapid quenching, except as noted for Sample A

B3 is prepared as Sample B2, then was reheated to 110°C at 5°C min^{-1} and held for 10 min, and finally quenched in LN_2-cooled glass beads.

All the samples were kept in a desiccator several days to minimize moisture pick-up. Figure 1 shows the scheme for the sample preparation, with heating/cooling rates between stages indicated.

Wide-angle X-ray scattering (WAXS) patterns of Nylon-6 films were obtained at room temperature on a Bruker AXS from $2\theta = 8–35°$ (for θ the half-scattering angle) at wavelength $\lambda = 0.1545$ nm. Scattered intensity was corrected for air background, and the two-dimensional isotropic pattern was converted to a one-dimensional pattern by integrating over a sector. The crystallinity index, χ_{ci}, was determined from the

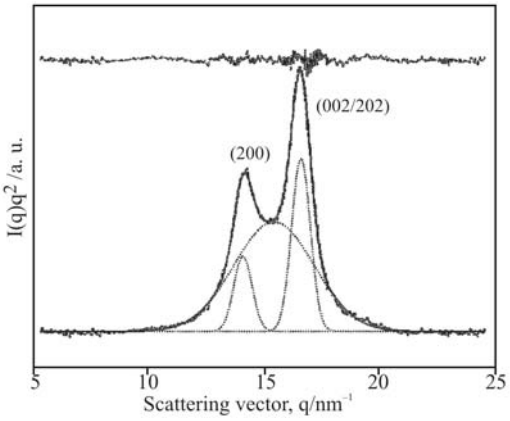

Fig. 2 Deconvolution of the Lorentz-corrected WAXS intensity, $I(q)q^2$ *vs.* q, using Gaussian wave functions for Nylon-6 sample A, after baseline subtraction. Dashed curve – experimental data; dotted lines – individual Gaussian components; solid line – summation of Gaussian peaks. Above the curves, the residual between the data and the summation of the Gaussian peaks is shown using a dash-dot line

Table 1 Thermal and X-ray parameters characterizing Nylon-6: glass transition temperature, heat capacity increment, crystalline, mobile amorphous, and rigid amorphous fractions

Sample	T_g^a/°C±0.2	ΔC_p/J g^{-1}K^{-1}±0.002	χ_c^b±0.01	χ_{ci}^c±0.01	χ_{MA}±0.01	χ_{RA}^d±0.02
A	45.4	0.147	0.33	0.34	0.31	0.36
B1	49.5	0.123	0.34	0.35	0.26	0.40
B2	42.1	0.207	0.34	0.35	0.44	0.23
B3	48.7	0.140	0.34	0.35	0.30	0.36

[a] Glass transition temperature determined from the inflection point of the heat capacity step at T_g, [b] Crystallinity obtained from DSC at 2°C min^{-1} using Eq. (2), [c] Crystallinity index obtained from WAXS at room temperature, [d] Obtained from Eq. (5) using a three-phase assumption

ratio between the crystalline peaks (found by subtraction of a scaled amorphous background) and the total area of coherent scattering. The Lorentz corrected intensity, Iq^2 (where q=4πsinθ/λ), was fitted by a sum of Gaussians and a quadratic baseline using:

$$I(q)q^2 = \Sigma \{A_i \exp((q-q_0)^2/2\sigma_i^2)\} + Bq + Cq^2 \quad (1)$$

where A_i is the amplitude, q_{0i} is the mean q-vector, σ_i the standard deviation, and B and C are the q and q^2 coefficients of the quadratic, respectively. Each peak was modeled using a Gaussian peak shape and fitted using a Nelder-Mead simplex direct search routing [20]. Figure 2 is an example of a diffraction curve from sample A that has been resolved into crystalline and amorphous scattering components using Gaussian peak shape. Three components were used, one to represent the amorphous halo, and two principal peaks of the alpha crystallographic phase having Miller Indices (200) and (002/202) [1]. The crystallinity indices for the four samples are listed in Table 1.

Real-time X-ray intensity data were collected in transmission mode at Brookhaven National Laboratory, National Synchrotron Light Source at the X27C beam line. Two one-dimensional, gas filled wire detectors were used for simultaneous WAXS and SAXS data collection. The wavelength (λ) was 0.1371 nm and the scattering vector, q(q=4πsin θ/λ), (for θ the half-scattering angle) was calibrated using silver behenate for SAXS, and sodelite and silicon for WAXS. For room temperature measurements, scattering patterns were recorded every 60 s or 600 s. For real-time measurement, the sample was heated from room temperature to the melting point at 5°C min^{-1} in a Mettler hot stage. Intensity was collected every 30 s during heating.

The raw intensity data, $I(q)$, were corrected for detector linearity, sample absorption, background scattering, and changes in incident beam intensity. The Bragg long period (L_B) was determined from the position of the peak in the Lorentz-corrected SAXS intensity, $I(q)q^2$.

TMDSC studies were carried out with a TA Instruments temperature modulated DSC (TA Q100). Indium was employed for the temperature and heat flow calibration. The heat capacity was evaluated with respect to sapphire standard. Dry nitrogen gas was purged into the TMDSC cell with a flow rate of 50 mL min^{-1}. All TMDSC measurements were performed at a heating rate of 2°C min^{-1} with temperature modulation amplitude of 0.318°C and temperature modulation period of 60 s. Three runs were taken to obtain the reversing heat capacity of all samples [9]. The first run is empty Al sample pan *vs*. empty Al reference pan to obtain baseline correction. The second run is sapphire standard *vs*. empty Al reference pan to calibrate heat flow amplitude. The third run is sample *vs.* the empty reference pan. All the empty Al reference pans and all the Al sample pans were kept the same in mass (m=23.88 mg). The sample mass was kept about 4–6 mg.

For the crystallinity measurements, a heat of fusion of ΔH_f=241 J g^{-1} was assumed for 100% crystalline Nylon-6 monoclinic alpha phase [1]. The degree of crystallinity χ_C was obtained from:

$$\chi_C = \Delta H_{f(meas)} / \Delta H_f \quad (2)$$

where $\Delta H_{f(meas)}$ is the measured heat of fusion, which was determined by integrating the endothermic heat flow from 150 to 250°C [1].

Results and discussion

Vitrification and de-vitrification of the rigid amorphous fraction

Figures 3a, b shows two examples of the reversing heat flow (R), total heat flow (T) and non-reversing heat flow (NR) curves obtained from the Samples A and B1, respectively. The curves are presented with the same scaling, but are displaced vertically for clarity. The glass transition step is seen to occur in the reversing heat flow curve at about 50°C in both samples. All four samples exhibited the glass transition relaxation and the melting endotherm process. Table 1 lists the values of T_g, heat capacity step at T_g, and the crystalline fraction, χ_c, deduced from the endotherm area using Eq. (2) for the four samples. The DSC-determined crystallinity, χ_c~0.34, for the

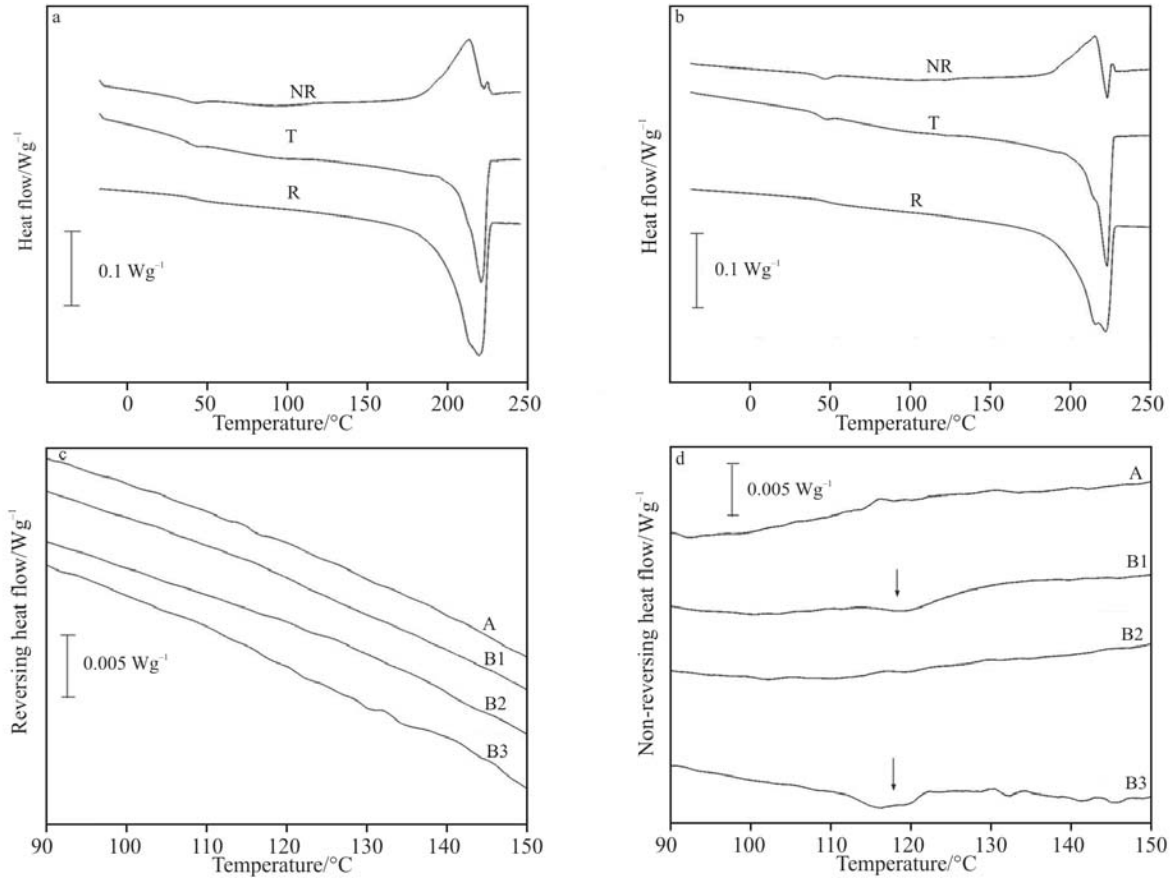

Fig. 3 TMDSC results for Nylon-6 samples obtained at 2°C min^{-1}: Total heat flow (T), Reversing heat flow (R), Non-reversing heat flow (NR). The curves are displaced vertically for clarity. a – Sample A; b – Sample B1; c – R curves in the vicinity of annealing peak for all samples as labeled; d – NR curves in the vicinity of T_a for all samples as labeled. Arrows in (d) show the location of the annealing peak

four samples are nearly the same within experimental error. The crystallinity indices from WAXS data, χ_{ci}~0.35, are systematically higher than the χ_c obtained from DSC, but confirm that the samples all have the same crystallinity. We conclude that the annealing treatments at 110°C, followed by brief heating to 136°C, and then re-annealing at 110°C, have no apparent impact on the degree of crystallinity of the type-B samples compared to the parent Sample A.

An examination of the four samples was made with respect to their behavior near the annealing peak. Figures 3c, d show the reversing and non-reversing heat flow, respectively, for all four samples. The reversing heat flow shows no features from 90 to 150°C. On the other hand, the non-reversing heat flow shows two annealing peaks for samples B1 and B3. We present in Figs 4a, b the derivatives of the reversing and non-reversing heat flow curves, respectively, from 20 to 160°C. The curves are presented with the same vertical scaling, but are displaced for clarity.

A peak in the derivative of the heat flow directly results from the inflection point occuring at T_g. In the reversing heat flow derivatives (Fig. 4a), all four samples have peaks with downward deflection in the vicinity of the glass transition (~50°C). A peak in the derivative R-curve arises from a sigmoid-type transition, like the glass transition, in the reversing heat flow curve. Near T_g, most samples (A, B1, B3) show downward-then-upward deflection in the non-reversing heat flow derivative curves (Fig. 3b). This feature in the derivative NR-curve arises from a peak in the non-reversing heat flow curve, most likely the result of some physical aging.

The major differences among the four samples can be seen in the vicinity of the annealing peak, above 110°C. In the reversing heat flow (Fig. 3c) and R-derivative curves (Fig. 4a) the four samples have no clear features between T_g and the melting endotherm. However, the non-reversing heat flow (Fig. 3d) and NR-derivative curve (Fig. 4b) shows two features in samples B1 and B3 only. There is an endothermic peak just above 110°C in Samples B1

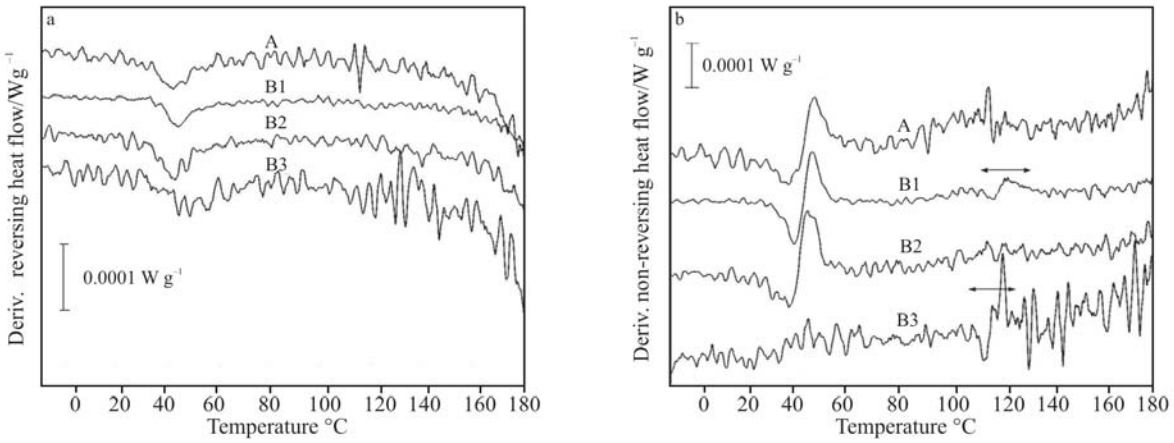

Fig. 4 Derivative of the a – reversing heat flow, b – non-reversing heat flow, for Nylon-6 samples as labeled. The horizontal arrow in b – marks the location of the annealing peak

and B3. Sample B2, which had been momentarily heated above the annealing peak, has no annealing peak feature in the non-reversing heat flow or its derivative curves. Thus, it appears that the annealing peak can be removed by briefly heating the sample to a temperature above T_a followed by fast cooling. Then, the annealing peak is restored by re-annealing Sample B3 at the same temperature as sample B1.

The fraction of the mobile amorphous phase (χ_{MA}) in crystalline Nylon-6 sample was calculated directly from the ratio of the heat capacity increment, ΔC_p^{sc}, of the semicrystalline sample to that of the wholly amorphous sample, ΔC_{p0}, at the glass transition, using [21]:

$$\chi_{MA} = \Delta C_p^{sc} / \Delta C_{p0} \qquad (3)$$

We were unable to obtain a measured ΔC_{p0} of wholly amorphous sample. The film quenched in LN_2 cooled glass beads crystallized immediately into the gamma phase during the TMDSC scan, producing an exotherm that masked the T_g step of the amorphous sample. Therefore, from the AHTAS data bank [22], the ΔC_{p0} of wholly amorphous sample was taken as 0.475 J g^{-1} K^{-1}.

Figure 5 shows the specific reversing heat capacity of sample B2. The dotted lines represent the values of C_p^{solid} and C_p^{liquid}, taken from the ATHAS data bank [22], which values agree well with the measured data for reversing heat capacity below T_g, and above the melting point, respectively. The dashed line represents the calculated heat capacity, C_p^{SC}, within a temperature range around T_g, under the assumption that all the MAF has relaxed to the mobile liquid state, and only the crystals and RAF remain in the solid state (i.e., $\chi^{solid}=\chi_c+\chi_{RA}$). The calculation uses [23]:

$$C_p^{SC}(T) = \chi^{solid}\, C_p^{solid}(T) + \chi_{MA}\, C_p^{liquid}(T) \qquad (4)$$

Data from Table 1, Sample B2, were used in the calculation (χ^{solid}=0.57) and from Fig. 5 we see that there is good agreement between the calculated line (dashed) and the measured data curve (solid line) immediately above the glass transition heat capacity step, and the slope of the calculated heat capacity lies between the slopes of the lines (dotted) for $C_p^{solid}(T)$ and $C_p^{liquid}(T)$.

Figure 6 shows the specific reversing heat capacity near T_g for all samples with expanded scaling. The ordinate values are correct only for B2, and the other curves are shifted vertically for clarity. The vertical line marks the location of the inflection point at T_g. The heat capacity increment is seen to increase in B2, the sample that was briefly heated to 136°C, and then decrease once again in B3, after re-annealing at 110°C. The χ_{MA} values determined from these data are included in Table 1.

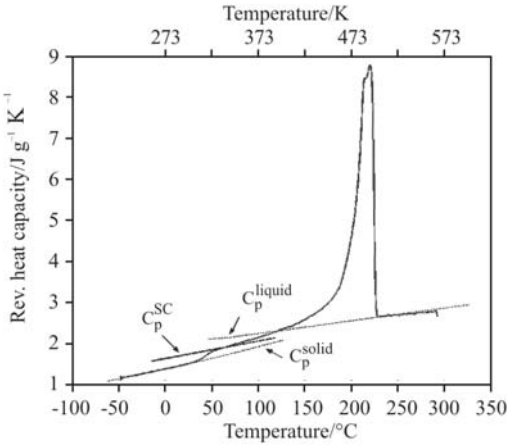

Fig. 5 Specific reversing heat capacity *vs.* temperature for Nylon-6 sample B2. C_p^{liquid} and C_p^{solid}, are the heat capacity of 100% liquid and 100% solid, respectively, obtained from ATHAS data bank [22]. $C_p^{calc}(T)$, is determined from Eq. (4) based on a solid fraction of 0.57

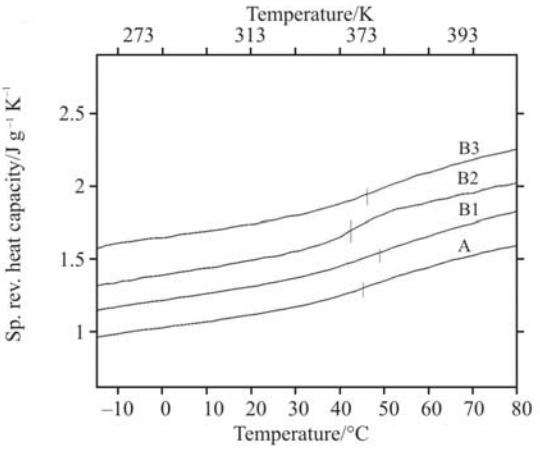

Fig. 6 Specific reversing heat capacity near T_g for Nylon-6 samples as marked. The ordinate scaling is correct only for sample B2; other curves are shifted vertically for clarity. The vertical lines mark the location of the inflection point at T_g

The fraction of the rigid amorphous phase, χ_{RA}, is calculated in the normal way from a three-phase assumption using [21, 23–25]:

$$\chi_{RA} = 1 - \chi_{MA} - \chi_C \quad (5)$$

here, we use the crystallinity determined from the DSC heating scan. The rigid amorphous fractions are listed in Table 1. We observe that the first annealing treatment at 110°C for Sample B1 causes the heat capacity increment at T_g to decrease, resulting in a smaller amount of mobile amorphous fraction and concomitant increase in RAF (χ_{RA}(B1)~0.40), in sample B1 compared to A. A major impact on the heat capacity increment is seen after the brief heating to 136°C, a temperature just above the annealing peak. Now the ΔC_p^{sc} increases substantially, leading to a large increase in mobile amorphous fraction, and reduction in RAF (χ_{RA}(B2)~0.23). Upon re-annealing sample B3 at the initial temperature of 110°C, the mobile amorphous fraction decreases and RAF increases. These changes in mobile amorphous and rigid amorphous fractions occur with no change in the apparent crystallinity of the treated samples.

There are similarities and differences to prior observations of creation and disappearance of the rigid amorphous fraction in other semicrystalline polymers. First, upon heating briefly above the annealing peak, the rigid amorphous fraction is greatly reduced. This is similar to what was observed in iPS [26], PPS [8], PHB and PC [12]. One important difference is that for iPS [26], PPS [8], PHB and PC [12], the RAF is completely devitrified when the temperature increases above the annealing peak. But for Nylon-6, not all of the RAF is devitrified upon brief heating above the annealing peak. A large rigid amorphous fraction, 0.23, still remains in the solid state after brief heating to 136°C. Thus, it appears that for Nylon-6, some RAF is associated with relaxation at the annealing peak, while another portion of RAF possibly relaxes at a much higher temperature.

For the other polymers above (iPS, PPS, PHB and PC), all the crystals and the RAF are established during annealing or isothermal cold crystallization from the glassy amorphous state, resulting in observation of an annealing peak. For Nylon-6, since the parent material (Sample A) was slowly cooled from the melt, both the crystals and a portion of the RAF has already formed before the annealing at 110°C. We suggest that annealing at 110°C just results in the densification of the amorphous phase, and an increase of RAF with no apparent change in crystallinity. For PPO [11], Wunderlich suggests the RAF will completely devitrify only when the crystallinity becomes zero. For PPO [11], the crystallinity is close to 0.30 and RAF is about 0.70. The RAF was established before annealing, and although annealing did affect the glass transition temperature, the RAF completely devitrifies only when the crystallinity becomes zero [11]. So we suggest that brief heating above the annealing peak can not totally eradicate the RAF, if a portion of it had been formed before at higher temperature, for example, during cooling from the melt. By reheating Nylon-6 to 110°C and holding for 10 min (Sample B3), the RAF increased once again while the crystallinity showed still no apparent change. Also there was no apparent change in the peak position in the derivative of the NR curve compared to the Sample B1. This is in agreement with the observation of Lu and Cebe for PPS [8]. The RAF fraction increases up to 36%, which is close to its value in Sample A. The portion of the RAF in Nylon-6, which was established only during the annealing at 110°C and disappears during brief heating to 136°C, is unstable, and can undergo vitrification once again, by re-annealing the sample.

Lamellar structural model for Nylon-6

In this portion of our research, we use X-ray scattering, combined with just-described thermal analyses, to permit a conclusion about the lamellar structural model which best describes Nylon-6. As mentioned in the Introduction Section, the two competing models are the Heterogeneous Stack Model, HET [14, 15], and the Homogeneous Stack Model, HSM [15–19]. Figures 7a and b show these two schematically, depicting crystals (C – light grey), rigid amorphous (R – dark grey) and mobile amorphous (M – white) layers. HET (Fig. 7b) makes the assumption that all of the mobile amorphous material is out-

Table 2 Crystalline, rigid amorphous and mobile amorphous volume fractions, Bragg long period, and phase thicknesses for Nylon-6*

Sample	Φ_C^a	Φ_{MA}^a	Φ_{RA}^a	L_B^b/nm ±0.05	L_C^c/nm ±0.05	L_{MA}^c/nm ±0.05	L_{RA}^d/nm ±0.05
A	0.31	0.32	0.37	9.54	2.92	3.06	3.56
B1	0.31	0.27	0.42	9.64	3.04	2.60	4.00
B2	0.31	0.45	0.24	9.63	3.03	4.29	2.30
B3	0.32	0.31	0.37	9.63	3.04	3.00	3.59

[a] Volume fractions were calculated from mass-fraction using Eq. (7), [b] Determined from SAXS measurements, [c] Calculated using HSM, where $L_i = L_B\Phi_i$ (i=1–3; 1=C, 2=MA, 3=RA), [d] Each crystal-amorphous interphase has a thickness of $L_{RA}/2$

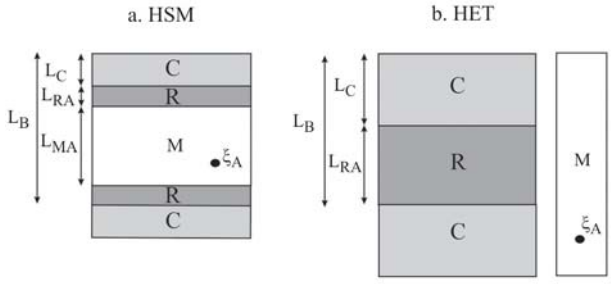

Fig. 7 Schematic representations of two structural models for semicrystalline polymer exhibiting lamellar structure: crystal lamella (C), rigid amorphous layer (R), mobile amorphous layer (M). L_B is the Bragg long period and ξ_A is the radius of the cooperatively rearranging regions (CRR). L_C, L_{MA}, L_{RA} are the thicknesses of the crystal lamella, mobile amorphous, and rigid amorphous layers, respectively. a – HSM; b – HET

side the lamella stack. In that case, the Bragg long period, L_B, comprises the crystal and the rigid amorphous fraction thicknesses, L_c and L_{RA}, respectively. The long period is written as L_B=L_C+L_{RA}. The implications of the HET lamellar model are that the cooperatively rearranging regions, CRR [27], of radius ξ_A, which contribute to the observed glass transition heat capacity step at T_g, are not located within the lamellar stacks. They are located in the non-crystalline regions (M) away from the stacks. PET is given as an exemplar of the HET-type polymer [14, 15] but this assignment has engendered some controversy [28–30]. In the HET model, we can obtain the L_c and L_{RA} using [15]:

$$L_C = L_B\,\Phi_c/(\Phi_C+\Phi_{RA}) \quad (6a)$$

$$L_{RA} = L_B\,\Phi_{RA}/(\Phi_C+\Phi_{RA}) \quad (6b)$$

where Φ_C, Φ_{RA}, Φ_{MA} are, respectively, the volume fractions of the crystalline, mobile amorphous, and rigid amorphous material.

HSM is shown in Fig. 7a. Here, the lamellar stacks are space-filling; there is no amorphous material located outside of the lamellar stacks. PBT was given as an example of a polymer described by the HSM [15]. In this model, the Bragg long period, L_B, comprises the crystal thickness, L_c, and the amorphous phase thickness, L_A, where L_B=L_C+L_A=L_C+L_{MA}+2L_{RA}. The location of the RAF is thought to be at the crystal amorphous interfaces [16–19]. In HSM, the interlamellar amorphous phase is the contributor to the glass transition step seen calorimetrically [16, 19]. The cooperatively rearranging regions contributing to T_g are located within the lamellar stacks in the mobile layer (M).

Figures 8a, b shows the results of SAXS experiments on Sample A. SAXS intensity data obtained at room temperature are shown in Fig. 8a. Nylon-6 has extremely weak SAXS scattering, and at room temperature the peak can be clearly seen only when the intensity is presented in logarithmic scaling. Figure 8b is the Bragg long period obtained upon heating sample A. The long period slowly increased from 9.6 to 10.4 nm until melting began at about 150°C. Within the range of our annealing temperatures, 110° and 136°C, the Bragg long period is constant. Corresponding WAXS results (data not shown) during heating indicate that only the alpha crystallographic phase is seen in any of our Nylon-6 samples.

Table 3 Thermal parameters for the Nylon-6: Glass transition temperature, transition width, volume and radius of cooperatively rearranging regions

Sample	T_g/°C±0.2	ΔT_g/°C±0.1	$V_A\times10^{-27}/m^3$±0.2	ξ_A/nm ±0.01
A	45.4	8.3	3.88	0.975
B1	49.5	9.1	3.13	0.908
B2	42.1	7.5	5.20	1.075
B3	48.7	8.7	3.52	0.944

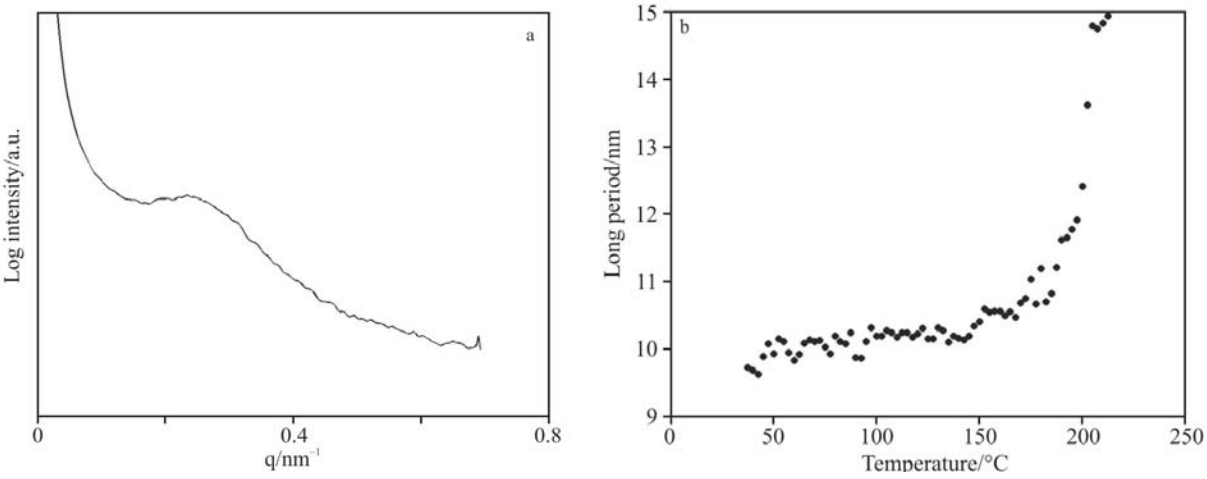

Fig. 8 Small angle X-ray scattering results for Nylon-6 Sample A. a – Log(I) *vs. q* at room temperature. b – Bragg long period *vs.* temperature during heating, determined from the position of the peak in (a) after background subtraction

The Bragg long periods of the four samples are listed in Table 2. The volume fraction of the crystalline (Φ_C), mobile amorphous (Φ_{MA}), and rigid amorphous (Φ_{RA}) phases were calculated from the mass fractions, χ_i, and densities, ρ_i (where i=1–3; 1=C, 2=RA, 3=MA) using:

$$\Phi_i = (\chi_i/\rho_i)/\Sigma\,(\chi/\rho_i) \qquad (7)$$

The assumption is made that the Φ_{RA} and Φ_{MA} have approximately the same density, ρ_a=1.100 g cm^{-3} [29]. The (alpha phase) crystalline phase density is ρ_c=1.23g cm^{-3} [31]. Volume fractions of each phase are listed in Table 2.

These volume fractions were used to determine the thicknesses of corresponding layers that contribute to the small-angle scattering profile, under either the HET or HSM. In HSM (Fig. 7a), the thickness of the crystalline layer can be obtained using L_C=$L_B\Phi_C$. In HET (Fig. 7b), L_c is found from Eq. (6a), L_C=$L_B\Phi_c/(\Phi_C+\Phi_{RA})$.

Our thermal and wide-angle X-ray measurements show that the crystalline fraction is unchanged by the annealing treatments applied here to Nylon-6 (Table 1). We therefore make the assumption that, no matter which model is correct, the lamellar thickness will not vary among the three annealed samples, and L_C(B1)=L_C(B2)=L_C(B3).

Hence, according to Eq. (6a) and our assumption of constancy of L_C, if the HET is correct then L_B(B1)>L_B(B2). This inequality arises because of the very large differences we measured in the values of Φ_{RA} (i.e., Φ_{RA}(B1)=0.415 compared to Φ_{RA}(B2)=0.239). As shown in Fig. 7b, a reduction in the rigid amorphous fraction in sample B2 (with no change of crystalline fraction) would reduce the R layer thickness. This would result in a decrease in the long period of sample B2. On the other hand, if the HSM is correct, then L_B(B1)=L_B(B2)=L_B(B3). From the measured long periods of our SAXS data in Table 2, we see that the long period does not vary among the Samples B1–B3. This allows us to conclude that the HSM is correct for Nylon-6. We note that L_B of Sample A is a little bit smaller than that of the other samples, but the reason is the crystallinity of Sample A is also a little bit smaller.

According to Schick and coworkers [19, 32], the cooperativity length (ξ_A) can be determined from thermal parameters. The radius (ξ_A) of cooperatively rearranging regions (CRR) [24] of (assumed spherical) volume (V_A) can be found from [19, 32]

$$V_A=k_BT_g^2\Delta(1/C_v)/(\delta T)^2\rho = (4\pi/3)\,\xi_A^3 \qquad (8)$$

where k_B is Boltzmann's constant, C_V is the specific heat calculated from C_p at the glass transition by Nernst equation, and ρ is the sample density. The mean temperature fluctuation (δT) is estimated from the width of the glass-transition step (ΔT) as [19, 30] δT~0.4 ΔT. For the four samples, the thermal parameters and calculated cooperativity length (ξ_A) are listed in Table 3. L_{MA} in Nylon-6 is always larger than 2ξ_A. ξ_A decreases with increasing of RAF while the crystallinity showed still no apparent change. The formation of RAF suppresses the large-mode length at the glass transition, leading to the broadening of the glass transition region and shift of T_g.

Conclusions

In this work, annealing semicrystalline Nylon-6 at a temperature above T_g results in an increase in the glass transition temperature and in the rigid amorphous fraction. An annealing peak appears in the non-reversing heat flow curve. Brief exposure to a temperature above the annealing peak causes a

de-vitrification of some of the rigid amorphous fraction, with no apparent change in crystallinity. These results suggest that the RAF is located within the amorphous phase. Devitrification, or non-reversing mobilization**,** of some RAF may be accompanied by melting of a small amount of imperfect crystals, which melt in the vicinity of the annealing peak, as suggested by Schick and co-workers [10]. However, brief heating above the annealing peak did not totally eradicate the RAF, suggesting that some portion of the RAF had been formed prior to the annealing at 110°C, most likely during the slow cooling stage. Reorganization or recrystallization of Nylon-6 takes place when the sample reaches the previous treatment temperature.

Using a combination of thermal analysis and structural techniques we are able to assign Nylon-6 to the category of polymers which exhibit homogeneous lamellar stacks, according to the HSM. In HSM, the Nylon-6 lamellar stacks comprise the crystal lamellae, two rigid amorphous layers near the lamellar surfaces, and a mobile amorphous layer. The CRR's are located within the mobile amorphous layer, where they are in proximity to the rigid amorphous layer. The cooperativity length (ξ_A) increases with a decrease of rigid amorphous fraction, or, increase of the mobile amorphous fraction. Devitrification of some of the RAF leads to the broadening of the glass transition region and shift of T_g.

Acknowledgements

The authors thank the National Science Foundation, Polymers Program of the Division of Materials Research, for support of this work through DMR-0602473.

References

1 T. D. Fornes and D. R Paul, Polymer, 44 (2003) 3945.
2 S. S. Pesetskii and B. Jurkowski, Eur. Polym. J., 41 (2005) 1380.
3 R. Schteiber and W. S. Veeman, Macromolecules, 32 (1999) 4647.
4 S. Y. Kwak and J. H. Kim, J. Polym. Sci., Polym. Phys. Ed., 38 (2000) 1285.
5 H. E. Miltner, Polymer, 47 (2006) 826.
6 M. Song, J. Appl. Polym. Sci., 81 (2001) 2779.
7 P. P. Huo and P. Cebe, Colloid Polym. Sci., 25 (1992) 902.
8 X. Lu and P. Cebe, Polymer, 37 (1996) 4857.
9 H. Xu and P. Cebe, Macromolecules, 37 (2004) 2797.
10 A. Minakov, D. Mordvintsev, R. Tol and C. Schick, Thermochim Acta, 442 (2006) 25.
11 J. Park, M. Pyda and B. Wunderlich, Macromolecules, 36 (2004) 495.
12 C. Schick, A. Wurm and A. Mohammed, Thermochim. Acta, 396 (2003) 119.
13 C. Schick, A. Wurm and A. Mohammed, Colloid Polym. Sci., 279 (2001) 800.
14 C. Alcarez and I. Sics, Polymer, 45 (2004) 3953.
15 B. B. Sauer and B. S. Hsiao, Polymer, 36 (1995) 2553.
16 B. Hahn and J. Wendorff, Macromolecules, 18 (1985) 718.
17 B. Hahn and V. Percec, Macromolecules, 20 (1987) 2961.
18 B. Natesan and P. Cebe, J. Polym. Sci., Poly. Phys. Ed., 42 (2004) 777.
19 C. Schick and E. Donth, Phys. Scr., 43 (1991) 423.
20 MATLAB™ The Mathworks, Natick, MA, 2000.
21 H. Suzuki, J. Grebowicz and B. Wunderlich, Br. Polym. J., 17 (1985) 1.
22 ATHAS data bank, http://web.utk.edu/athas/databank/amide/nylon6/, Ed., M. Pyda, 1997.
23 V. B. F. Mathot, Calorimetry and Thermal Analysis of Polymers, Hanser Gardner Publications, Inc., Cincinnati, 1994.
24 B. Wunderlich, J. Therm. Anal. Cal., 85 (2006) 179
25 J. Park, W. Qui and M. Pyda, J. Therm. Anal. Cal. 82 (2005) 565.
26 H. Xu and P. Cebe, J. Polym Sci, Poly. Phys. Ed., 42 (2004) 777.
27 G. Adam and J. H. Gibbs, J. Chem. Phys., 43 (1965) 139.
28 A. M. Jonas and T. P. Russell, Macromolecules, 28 (1995) 8491.
29 C. Fougnises and Dosiere, Macromolecules, 31 (1998) 6226.
30 H. G. Haubruge and A. M Jonas, Macromolecules, 37 (2004) 126.
31 N. Vasanthan, J. Polym. Sci., Poly. Phys. Ed., 41 (2003) 2870.
32 J. Dobbertin, A. Hensel and C. Schick, J. Therm. Anal. Cal., 47 (1996) 1027.

DOI: 10.1007/s10973-007-8215-4